Plastic deformation of polycrystals of $Co_3(Al,W)$ with the $L1_2$ structure

Norihiko L. Okamoto,[1,†] Takashi Oohashi,[1] Hiroki Adachi,[1] Kyosuke Kishida,[1] Haruyuki Inui,[1] and Patrick Veyssière[2]

[1] *Department of Materials Science and Engineering, Kyoto University, Kyoto 606-8501, Japan*
[2] *Laboratoire d'Etude des Microstructures, CNRS-ONERA, BP 72, 92322 Châtillon cedex, France*

[†] Corresponding author:
Norihiko L. Okamoto
Department of Materials Science and Engineering, Kyoto University
Sakyo-ku, Kyoto 606-8501, Japan
Tel: +81-75-753-5481
Fax: +81-75-753-5461
Email: n.okamoto@at4.ecs.kyoto-u.ac.jp

(Received XX XXXX 2011; final version received XX XXXX 2011)

The plastic behaviour of $Co_3(Al,W)$ polycrystals with the $L1_2$ structure has been investigated in compression from 77 to 1273 K. The yield stress exhibits a rapid decrease at low temperatures (up to room temperature) followed by a plateau (up to 950 K), then it increases anomalously with temperature in a narrow temperature range between 950 and 1100 K, followed again by a rapid decrease at high temperatures. Slip is observed to occur exclusively on {111} planes at all temperatures investigated. The rapid decrease in yield stress observed at low temperatures is ascribed to a thermal component of solid-solution hardening that occurs during the motion of APB-coupled dislocations whose core adopts a planar, glissile structure. The anomalous increase in yield stress is consistent with the thermally activated cross-slip of APB-coupled dislocations from (111) to (010) as for many other $L1_2$ compounds. Similarities and differences in the deformation behaviour and operating mechanisms among $Co_3(Al,W)$ and other $L1_2$ compounds, such as Ni_3Al and Co_3Ti, are discussed.

Keywords: intermetallic compound; Co-base superalloys; compression deformation behaviour; dislocation; transmission electron microscopy

1. Introduction

The ever-increasing demands for structural materials that can withstand severe oxidizing environments and high operating temperatures have led to the discovery of a new stable ternary $L1_2$ phase that can coexist with a face-centered cubic (fcc) solid-solution based on cobalt, referred to as γ' and γ phases, respectively [1]. Although serious doubt has recently been cast upon the thermal stability of the ternary $L1_2$ phase [2], this discovery has triggered extensive worldwide research activities on the development of a new class of high-temperature Co-based structural material known as 'Co-based superalloys' [3-6], since γ+γ' two-phase microstructures resembling those in Ni-based superalloys have been shown to form in ternary and some quaternary alloys [1,3-6]. Phase equilibria of the ternary and higher-order systems near the γ+γ' two-phase region [1-2,5,7] in addition to plasticity of γ+γ' two-phase alloys in compression [3-4,6] and in tensile creep [8] have been investigated. Based on the assumption that the ternary $L1_2$ compound in Co-Al-W-based alloys exhibits physical properties similar to those of Ni_3Al-based compounds in Ni-based superalloys, the current study was carried out in the hope that the mechanical properties of Co-Al-W-based alloys would be similar to those of Ni-based superalloys. Yet almost nothing is known about the mechanical properties of the ternary $L1_2$ compound, $Co_3(Al,W)$, in single phase form.

Tanaka et al. [9] reported that both single-crystal and polycrystalline $Co_3(Al,W)$ are elastically stiffer than $Ni_3(Al,Ta)$. The elastic anisotropy factor of $Co_3(Al,W)$ is also the largest of both alloys [9]. From the ratio of shear to bulk modulii, Poisson's ratio and Cauchy pressure, Tanaka et al. [9] also suggested that $Co_3(Al,W)$ may exhibit some ductility, in contrast to the prediction from first principles calculations by Yao et al. [10]. Miura et al. [11] reported from compression tests on $L1_2$ $Co_3(Al,W)$ polycrystals that, unlike Ni_3Al, yield stress exhibits a modest positive temperature dependence at high temperatures above 1000 K. Although no compression test was conducted below room temperature, they suggested that the temperature dependence of the yield stress of $Co_3(Al,W)$ is similar to that of Co_3Ti [11]. There have been studies on dislocation-related deformation mechanisms in γ+γ' two-phase alloys in the Co-Al-W system [3-4]; however, no detailed study is available on local dislocation mechanisms in $Co_3(Al,W)$ in single phase form with respect to the various deformation stages of this alloy.

In the present study, we investigate the compression behaviour of polycrystals of $L1_2$ $Co_3(Al,W)$ between 77 K and 1273 K and we characterize the main deformation

microstructures with the aim of ascertaining the origins of the similarities and differences between the properties of $Co_3(Al,W)$ and those of other $L1_2$ compounds.

2. Experimental procedures

Ingots with a nominal composition of Co-12 at.%Al-11 at.%W were prepared by arc-melting high-purity Co, Al and W under an Ar gas flow. These ingots were sealed in a quartz ampoule with argon gas and annealed at 1123 K for 168 h followed by furnace cooling. Microstructures and chemical compositions of the phases present in the annealed ingots were examined by scanning electron microscopy (SEM) and energy dispersive x-ray spectroscopy (EDS). A typical SEM backscattered electron image (BEI) of the microstructure in an annealed ingot is shown in fig. 1. Although a small amount (8 % by volume) of additional phases, CoAl and Co_3W, were observed, the main phase was $Co_3(Al,W)$ with the $L1_2$ structure, which is consistent with the phase diagram assessment of Sato et al. [1]. The grain size of the $Co_3(Al,W)$ phase ranged from 200 to 1000 μm. Transmission electron microscopy (TEM) observations of as-annealed ingots indicated that the $Co_3(Al,W)$ phase actually crystallized under the ordered $L1_2$ structure and that the microstructure was free from thermal anti-phase boundaries (APBs).

Specimens with dimensions $1.8\times1.8\times5$ mm^3 were cut from the annealed ingots by electro-discharge machining. Their faces were mechanically polished with SiC paper and then electrochemically polished in a solution of perchloric acid, buthanol and methanol (1:6:12, v/v) at 233 K and 18 V. Compression tests were conducted on an Instron-type testing machine from 77 to 1273 K at a strain rate of 10^{-4} s^{-1}. Compression tests at low temperatures were performed with a specimen immersed in liquid nitrogen (77 K) or chilled ethanol (159 K), while tests above room temperature were carried out in vacuo. The operative slip planes were determined by slip trace analysis on two orthogonal surfaces of coarse grains whose crystal orientations were determined by electron backscattered diffraction (EBSD). Dislocation structures were examined with a JEM-2000FX TEM operated at 200 kV. Thin foils for TEM observations were cut parallel to the {111} macroscopic slip plane identified on a coarse grain and subjected to twin-jet electro-polishing in the above-described solution at 243 K and 18 V.

3. Experimental results

3.1. Stress-strain behaviour and slip trace analysis

Figure 2 shows typical stress-strain curves obtained with $Co_3(Al,W)$ polycrystals deformed at various temperatures. In compression, $Co_3(Al,W)$ exhibits significant ductility at all deformation temperatures, as expected from the single-crystal elastic constants of $Co_3(Al,W)$ [9]. The values of yield stress deduced as the 0.2% off-set flow stress are plotted in fig. 3 as a function of temperature. Yield stress decreased rapidly with increasing temperature up to room temperature and more slowly up to approximately 950 K. Then, the yield stress increases anomalously with increasing temperature in a very narrow temperature range between 950 and 1100 K and decreased again at high temperatures. The curve is drawn as a guide for the eye and the three distinct temperature regions are designated I (77−950 K), II (950−1100 K) and III (above 1100 K) throughout this paper.

Deformation markings observed on two orthogonal faces of two different grains A and B in a specimen deformed at 77 K to a plastic strain of about 2 % are depicted in figs. 4(a)-(d), respectively. As determined by EBSD, the compression axes of grains A and B are approximately along [$\bar{3}$ 10 30] and [$\bar{7}$ 15 16], respectively (fig. 4(e)). In both grains, deformation proceeds by single slip on (111) which, in addition, is the exclusive operative deformation mode at 77 K over the wide range of grain orientation plotted in the stereographic projection of fig. 4(e). Slip trace analysis was similarly carried out on specimens deformed at different temperatures as exemplified in fig. 5 for selected temperatures (873, 1073 and 1173 K). The compression axis orientations of the grains investigated are plotted in the stereographic projections (figs. 5(c), (f) and (i) for 873, 1073 and 1173 K, respectively). In brief, slip operates exclusively on (111) at all temperatures and for all crystal orientations investigated.

3.2. Dislocation structures

3.2.1. Region I (77−950 K)

Figures 6(a)-(d) shows typical dislocation structures observed in specimens deformed in region I at 77, 159, 300 and 573 K, respectively. The dislocations are smoothly curved in their slip planes with no preferred orientations. Hence, the dislocations should not be on the bottom of Peierls valleys except for the faulted dipoles

(arrows) which can be observed especially at low deformation temperatures. A contrast analysis of the smoothly curved dislcations will be provided in the next paragraph to determine the dissociation scheme. The density and size of the faulted dipoles decrease with increasing deformation temperature up to 573 K, where the faulted dipoles disappear.

The dissociation scheme of dislocations exemplified in a specimen deformed at 77 K is analysed in fig. 7. A two-fold dissociation is observed along the dislocations imaged in figs. 7(a) and (b) under $\boldsymbol{g}$ (reflection vectors) = $20\bar{2}$ and $\bar{2}02$, respectively. The reversal of the peak asymmetry upon reversing $\boldsymbol{g}$ (see insets) is consistent with a dissociation of a dislocation with $\boldsymbol{b}$ (Burgers vector) = $[10\bar{1}]$ into two partials with collinear Burgers vectors $\boldsymbol{b}_p = 1/2[10\bar{1}]$ separated by an anti-phase boundary (APB) [12] on the (111) slip plane. The dissociation mode is confirmed by the fact that both partials are simultaneously out of contrast when imaged with $\boldsymbol{g} = 1\bar{1}1$ (fig. 7(c)) and $\boldsymbol{g} = 020$ (fig. 7(d)). Essentially the same results are obtained at all temperatures within region I. The apparent dissociation widths between superpartial dislocations at 77 K are corrected using the image shift correction method of Cockayne [13] and the polycrystalline shear modulus [9]. The corrected dissociation widths are plotted in fig. 8 as a function of dislocation line direction with respect to the Burgers vector. The three dashed curves in fig. 8 are derived from the DISDI program [14] which incorporates the alloy's elastic anisotropy. From the plot of fig. 8, the APB energy on (111) ($\gamma_{APB}^{(111)}$) is estimated as 155±20 mJ/m^2.

A magnified weak-beam image of a faulted dipole indicated by a double arrow in fig. 6(b) is shown in fig. 9(a). The faulted dipole is formed on the dislocation dissociated as determined above, and, according to curvature, moving from right to left. Dislocations L and T bounding the faulted dipole are invisible when imaged with $\boldsymbol{g} = 2\bar{2}0$ (fig. 9(b)) and $\boldsymbol{g} = 0\bar{2}2$ (fig. 9(c)), indicating Burgers vectors parallel to $[11\bar{2}]$ and $[2\bar{1}\,\bar{1}]$, respectively. Since the parent dislocation's Burgers vector is $[10\bar{1}]$, the Burgers vectors of the bounding dislocations L and T are necessarily $1/3[11\bar{2}]$ and $1/3[2\bar{1}\,\bar{1}]$, respectively. Fig. 9(c) also clearly shows at least one of the short dislocation segments that separate the APB and the stacking fault (white arrow). The nature of the stacking fault (with a displacement vector either +1/3[111] (intrinsic) or –1/3[111] (extrinsic)) was determined by comparison between experimental and simulated images (fig. 10). The images in the first row of fig. 10 correspond to experimental bright- and dark-field images of a faulted dipole taken with $\boldsymbol{g} = \pm 1\bar{1}\,\bar{1}$ in a thin foil cut from a specimen deformed at 77 K. The normal to the thin foil is approximately $[4\ \bar{1}\ 10]$ and the stacking fault (111) habit plane is inclined to the foil surface. The images in the

second/third and fourth/fifth rows are the corresponding images calculated on the assumption that the displacement vector ($\boldsymbol{R}_F$) is either +1/3[111] (intrinsic) or –1/3[111] (extrinsic), respectively. The two partial dislocations bounding the stacking fault are assumed to have the same Burgers vector ($\boldsymbol{b}$ = 1/3[11$\bar{2}$] and 1/3[$\bar{1}\,\bar{1}$2] for the second/fourth and third/fifth rows, respectively) and opposite line vectors ($\boldsymbol{\xi}$ = [11$\bar{2}$] and [$\bar{1}\,\bar{1}$2] for the upper and lower partial dislocations, respectively). A comparison of the experimental and calculated images indicates that the fault is a superlattice intrinsic stacking fault (SISF) with $\boldsymbol{R}_F$ = +1/3[111] and that the Burgers vector of the bounding dislocations is $\boldsymbol{b}$ = 1/3[11$\bar{2}$] [15]. Clearly, the faulted dipoles under consideration are unstable configurations, which should spontaneously annihilate unless opposed by a significant lattice friction applied to the curved tips and that adds to the Peierls stress onto the elongated portions. This would be consistent with the thermally activated disappearance of the faulted dipoles above room temperature. The issue of the formation mechanism of SISF bounding faulted dipoles in $Co_3(Al,W)$ as well as in other $L1_2$ alloys has never been elucidated.

3.2.2. Region II (950−1100 K)

Figures 11(a) and (b) show typical dislocation structures observed in specimens deformed at 973 and 1073 K, respectively, both of which belong to region II. In contrast to the case of region I, dislocations have a strong tendency to be aligned with their screw orientation. After deformation for example at 973 K and, as in the case of region I, dislocations with $\boldsymbol{b}$ = [10$\bar{1}$] are dissociated into two collinear superpartials with $\boldsymbol{b}$ = 1/2[10$\bar{1}$] separated by an APB along the screw orientation (fig. 12(a)). Both partials are indeed simultaneously invisible when imaged with $\boldsymbol{g}$ = $\bar{1}1\bar{1}$ (fig. 12(b)) and $\boldsymbol{g}$ = 020 (fig. 12(c)). Tilting the specimen about the [10$\bar{1}$] screw direction under $\boldsymbol{g}$ = 20$\bar{2}$ clearly indicates that the projected dissociation width of the screw segments is the largest when projected along the [010] direction (fig. 13); thus indicating that the locking is associated with complete or near-complete Kear-Wilsdorf locks. This behaviour is entirely similar to the microstructural signature of the positive temperature dependence of the yield stress in Ni_3Al- [16-18] and Co_3Ti-based [19] $L1_2$ compounds. On the assumption that the Kear-Wilsdorf type configuration observed in fig. 13 is of the complete type, i.e. the APB lies fully on (010), the APB energy on (010) ($\gamma_{APB}^{(010)}$) amounts to approximately 103 mJ/m^2 (fig. 13(a)). On the upper screw segments as well as on the bottom screw portion, the presence of several small kinks, known as APB

jumps [20] should be noted since it confirms the similarity between deformation of Co_3Ti- and Ni_3Ga-based $L1_2$ compounds and, by extension, of Ni_3Al-based alloys.

Of significance in fig. 12 is the observation that the curved segments, actually superkinks, connecting the locked screw portions, exhibit four-fold dissociation (fig. 12(d)); thus corresponding to the sub-dissociation of each superpartial dislocation with $\boldsymbol{b} = 1/2[10\bar{1}]$ into Shockley partials bordering a complex stacking fault (CSF). The widths of APB and CSF measured along the pure edge segment are approximately 6.0 and 4.2 nm, respectively, corresponding to fault energies of $\gamma_{APB}^{(111)}$=146 mJ/m^2 and $\gamma_{CSF}^{(111)}$=137 mJ/m^2). The APB energy on (111) obtained at 973 K (region II) is only slightly smaller than that obtained at 77 K (region I).

3.2.3. Region III (above 1100 K)

A typical dislocation structure observed in a specimen deformed at 1173 K is shown in fig. 14(a). Dislocations are observed to lie on the (111) slip plane with a much weaker tendency to be aligned along their screw orientation than in region II. A close look at the microstructure under $\boldsymbol{g}$ = 001 (fig. 14(b)) reveals the existence of thermal APBs, which are absent in the specimen before deformation. The existence of thermal APBs is a clear indication that the deformation temperature of 1173K is within the temperature range where the stable phase is the disordered fcc γ phase. Thermal APBs are then formed during the reordering that occurs during the cooling after deformation. The dislocations are curved in places to combine with the thermal APBs. Unlike many other Ni_3Al- [21-22] and Co_3Ti-based [23] $L1_2$ compounds, where high deformation temperature proceeds by slip on (010), the rapid decrease in yield stress at high temperatures of the present $L1_2$ compound is considered to be due to the transformation from the γ' to γ phases. In other words, the transformation from γ' to γ phases occurs in the present $L1_2$ compound before slip on (010), if possible, starts to operate.

4. Discussion

4.1. Temperature dependence of the yield stress

$L1_2$ alloys exhibit two separate regimes, i.e. either a positive or a negative temperature dependence of the yield stress. The positive and negative temperature dependences are accompanied by specific mechanical properties such as orientation dependence and strain rate sensitivity, respectively. These specific properties confer a

rather distinct signature on the system. We take advantage of the fact that the present system exhibits the two distinct regimes in a wide range of temperature to refine the analysis of the possible origins of the flow stress anomaly(ies).

With increasing test temperature above 77 K, the yield stress of $Co_3(Al,W)$ exhibits a rapid decrease at low temperatures followed by a near-plateau and an anomalous increase between 950 and 1100 K. As pointed out by Miura et al. [11], such a temperature dependence differs from that reported for Ni_3Al-based $L1_2$ compounds [21-22] but shows certain similarities with that observed for Co_3Ti [23-24]. Other differences to Ni_3Al-based $L1_2$ alloys are also noted [23-24] such as the onset temperature of the anomalous yield stress increase, which is significantly higher, and the temperature extent of the anomaly, which is considerably narrower in $Co_3(Al,W)$. Additionally, differences in deformation mechanisms between selected $L1_2$ compounds, including $Co_3(Al,W)$, Ni_3Al-based alloys and Co_3Ti, make it somewhat meaningless to classify $L1_2$ compounds only in terms of their yield stress–temperature curves.

4.2. Rapid decrease in yield stress at low temperatures

The rapid negative temperature dependence of the yield stress observed at low temperatures in $L1_2$ compounds, such as Co_3Ti [23-24] and Pt_3Al [24-25], is usually interpreted in terms of the thermally activated glide of SISF-coupled dislocation partials ($\boldsymbol{b}$ = 1/3<112>) whose core is believed to be non-planar, and hence, subject to lattice friction [26]. In the present work, we show that a similarly negative temperature dependence takes place in region I of $Co_3(Al,W)$ (Fig. 3) where dislocations are APB-coupled. Since dislocations exhibit no preferred crystalline orientations at low temperatures, the APB-coupled dislocations in $Co_3(Al,W)$ are glissile having a planar core structure. We are, thus, led to hypothesize an extrinsic cause of the negative flow stress dependence and, more specifically, the thermal component of solid-solution hardening. This effect is difficult to prove directly in $L1_2$ $Co_3(Al,W)$ because neither the composition dependence nor the orientation dependence of the yield stress can be investigated due to the very narrow compositional range of stability of the $L1_2$ phase and the difficulty to grow single crystals.

It is worth emphasizing, on the one hand, that single crystals of Co_3Ti [23] and $L1_2$-modified Al_3Ti [27] exhibit no significant orientation dependence in the low temperature domain of negative temperature dependence. On the other hand, the temperature dependence of Co_3Ti becomes highly composition dependent as the alloy

deviates from the stoichiometric composition [24]. Hence, certain mechanical properties of Co_3Ti and of $L1_2$-modified Al_3Ti are consistent with solid-solution hardening too. In other words, it may well be that the negative temperature dependence of the yield stress exhibited by Co_3Ti and $L1_2$-modified Al_3Ti is primarily controlled by solid solution hardening, even though deformation proceeds by glide of SISF-coupled partial dislocations ($\boldsymbol{b}$ = 1/3<112>) with a non-planar core.

The low temperature yield stress (τ_{SSH}) of at least $Co_3(Al,W)$ consists of an athermal (τ_{ath}) and a thermal (τ_{th}) component (fig. 15), such that [28-29]:

$$\tau_{SSH} = \tau_{ath} + \tau_{th}\left(1 - aT^{1/q}\right)^{1/p} \qquad (0 < p < 1,\ 1 < q < 2), \tag{1}$$

where T stands for the absolute temperature, and a, p and q are numerical constants. As far as $L1_2$ $Co_3(Al,W)$ is concerned, the values of τ_{ath} and τ_{th} amount to 273 and 370 MPa, respectively, with a = 0.0242, p = 0.5 and q = 1.5. Both the athermal and thermal components increase with solute concentration giving rise to a larger temperature dependence of the yield stress at low temperatures. Applied to Co_3Ti single crystals, Equation (1) indicates that the athermal and thermal components would increase from 27 to 35 MPa and from 45 to 80 MPa, respectively, as alloy composition changes from Co-22 at.%Ti to Co-21 at.%Ti [23].

Insofar as dissociation schemes in Co_3Ti are concerned, it is not entirely clear from the literature whether dislocations are actually SISF-coupled [30]. On the other hand, APB- and SISF-coupled dislocations seem to coexist in $L1_2$-modified Al_3Ti [31]. Specific observations are under progress in these $L1_2$ compounds in order to confirm the actual dissociation modes. In $Co_3(Al,W)$, SISFs are observed only as faulted dipoles formed onto APB-coupled dislocations. Although the density of faulted dipoles tends to decrease with increasing temperature, this may not have a direct consequence regarding the rapid decrease in yield stress [18]. Care has to be taken in TEM contrast interpretations to avoid misinterpreting a faulted dipole as a SISF-coupled dislocation, especially when the foil surface is inclined relative to the slip plane and the stacking fault contrast is visible while the dislocation line contrast is difficult to discern. In view of the comparable fault energies for $\gamma_{APB}^{(111)}$ and $\gamma_{CSF}^{(111)}$, the SISF energy ($\gamma_{SISF}^{(111)}$) is expected to be small [21]. This is consistent with the fact that DO_{19}-Co_3W, which can be formed by introducing SISFs periodically in the $L1_2$ structure, can exist in equilibrium with the present $L1_2$ compound, $Co_3(Al,W)$. The low value of $\gamma_{SISF}^{(111)}$ is

generally believed to favour dislocation dissociation of the SISF-type rather than of the APB-type [32]. The present observation of extensive APB-type dissociation, however, clearly indicates that SISF-type dissociation is not favoured only in terms of the low value of $\gamma_{SISF}^{(111)}$.

4.3. Anomalous increase in yield stress at high temperatures

In the temperature range of the yield stress anomaly, dislocations in $Co_3(Al,W)$ have a strong tendency to align parallel to their screw orientation as they do in many $L1_2$ Ni_3Al- [16-18] and Co_3Ti-based compounds [19]. Screw segments are locked in the Kear-Wilsdorf configuration that consists in two 1/2<110> partials coupled by an APB on a {010} plane. The Kear-Wilsdorf segments are interconnected by superkinks with mixed character. The anomalous yield stress increase observed in $L1_2$ $Co_3(Al,W)$ is, therefore, entirely consistent with the thermally-activated cross-slip of APB-coupled dislocations from (111) to (010). However, the question arises as to why the yield stress of $Co_3(Al,W)$ increases only at a very high temperature of 950 K, which is in striking contrast with the case of many Ni_3Al-based $L1_2$ compounds whose yield stress increases at a temperature as low as 77 K [16-17,21-22,33].

The anomalous strengthening component (τ_{AS}) adds to the athermal component (fig. 15) and can be expressed as

$$\tau_{AS} = \tau_{AS}' exp(-\Delta H/RT), \tag{2}$$

where τ_{AS}' is a constant, R the gas constant and ΔH the activation energy of the anomalous strengthening. From Equation (2), the onset temperature for the anomalous strengthening increases with ΔH. As for the $L1_2$ $Co_3(Al,W)$ compound under investigation, ΔH would amount to 123 kJ/mol, which is one order of magnitude higher than the values of 10-20 kJ/mol usually determined in most Ni_3Al-based $L1_2$ compounds. Such a large ΔH value clearly reflects the difficulty of cross-slip from (111) to (010). This now raises the question as to why cross-slip is so difficult in $Co_3(Al,W)$ compared to say Ni_3Si- and Ni_3Al-based $L1_2$ compounds. In the following, we discuss this point in terms of the anisotropy in APB energies ($\gamma_{APB}^{(111)}/\gamma_{APB}^{(010)}$), the elastic anisotropy factor and the CSF energy ($\gamma_{CSF}^{(111)}$).

One component of the driving force for cross-slip is believed to arise from the anisotropy of APB energies. Cross-slip is facilitated by large $\gamma_{APB}^{(111)}/\gamma_{APB}^{(010)}$ ratios. The ratio for the present $L1_2$ compound measured at 973 K is 1.42, which compares well

with those usually observed for many other $L1_2$ compounds based on Ni_3Al [18]. Thus, the anisotropy in APB energies should not be responsible for the observed temperature shift. Cross-slip is also believed to be promoted by the torque force acting on the two coupled screw partials [34]. The larger the elastic anisotropy factor ($A = 2c_{44}/(c_{11}-c_{12})$), the larger the torque. Our measurements of single-crystal elastic constants indicate that the anisotropy factor of the present $L1_2$ compound is larger than those of Ni_3Al-based $L1_2$ compounds by only 5 to 10% [9]. Hence, this possible origin cannot account for the temperature shift either. Finally, cross-slip of APB-coupled dislocations from (111) to (010) is expected to become more difficult as the CSF energy is lowered. Because the constriction energy increases, the onset temperature for the anomalous strengthening and, thereby, the ΔH value increases. $\gamma_{APB}^{(111)}$ and $\gamma_{CSF}^{(111)}$ measured in the present $L1_2$ compound are not so much different from those (147 and 177 mJ/m^2, respectively) estimated by Hemker and Mills [35] in Ni_3Al with a composition of Ni-24 at.%Al, in which the anomalous increase in yield stress is already noted at room temperature. Hence, the relatively low CSF energy determined in $L1_2$ $Co_3(Al,W)$ does not seem to play a decisive role in increasing the ΔH value and the onset temperature for the anomalous strengthening. The reasons for the high onset temperature for the anomalous strengthening and the high ΔH value in Equation (2) noted for the present $L1_2$ compound including the physical meaning of ΔH itself, thus, need further detailed investigation.

The high onset temperature for the anomalous strengthening indicates that the high-temperature strength of the present $L1_2$ compound, $Co_3(Al,W)$ is not so high when compared to Ni_3Al-based $L1_2$ compounds. This is detrimental to high-temperature creep properties of γ+γ' two-phase Co-based alloys with coherent cuboidal γ' precipitates, as our preliminary investigation of creep deformation of γ+γ' two-phase Co-based alloys indicated [8]. A reduction in the onset temperature for the anomalous strengthening has to be achieved to improve the high temperature strength of both the present $L1_2$ compound and γ+γ' two-phase Co-based alloys. Of interest to note is that this is reported to be achieved for binary Co_3Ti polycrystals by changing the alloy composition [24]. It was reported that the onset temperature for the anomalous strengthening decreased from 850 K for Co-18.5 at.%Ti to 700 K for Co-23.7 at.%Ti, although the change in the onset temperature is not so significant when tested with single crystals [23]. This may, however, be very difficult to achieve for the present compound, since the stable composition range of the $L1_2$ phase in the Co-Al-W ternary system is very much limited [1,7]. Instead, the anomalous temperature range can be extended towards

the high temperature side, since the upper bound of the anomalous temperature range is proved to be limited by the γ' solvus temperature. Studies on the phase equilibria [1,7] have indicated that additions of Ta, Ti and Nb in the amount of several at.% augment the γ' solvus temperature by 50-100 K. The effects of Ta additions on the extension of the anomalous temperature range for $Co_3(Al,W)$-based $L1_2$ compounds are currently under survey in our group.

5. Conclusions

(1) The yield stress of the present $L1_2$ compound, $Co_3(Al,W)$ exhibits a rapid decrease at low temperatures (up to room temperature) followed by a plateau (up to 950 K), then it increases anomalously with the increase in temperature in a narrow temperature range from 950-1100 K, followed again by a rapid decrease at higher temperatures. Slip is observed to occur exclusively on (111) octahedral planes at all temperatures investigated.
(2) The rapid decrease in yield stress observed at low temperatures is ascribed to a thermal component of solid-solution hardening, which in $Co_3(Al,W)$ occurs during the motion of APB-coupled dislocations with a planar and glissile core structure, in place of the expected thermally activated motion of SISF-coupled dislocations with a non-planar and sessile core.
(3) The anomalous increase in yield stress observed in the narrow temperature range 950-1100 K is ascribed to the thermally activated cross-slip of APB-coupled dislocations from (111) to (010), as in the case of many other $L1_2$ compounds. Accordingly, dislocations observed in this temperature range have a strong tendency to align parallel to their screw orientation with screw segments being locked in the Kear-Wilsdorf configuration and connected with each other by superkinks with edge components. The reason for the high onset temperature for anomalous strengthening has yet to be clarified.
(4) The anomalous temperature region is terminated by the γ' solvus temperature, above which slip occurs on (111) in the disordered fcc γ phase.

Acknowledgements

This work was supported by Grant-in-Aid for Scientific Research (A) (No.21246101 and No.21360337) from the Ministry of Education, Culture, Sports, Science and Technology (MEXT) Japan and in part by the Global COE (Center of Excellence) Program of International Center for Integrated Research and Advanced Education in Materials Science from the MEXT Japan.

References

[1] J. Sato, T. Omori, K. Oikawa, I. Ohnuma, R. Kainuma, and K. Ishida, Science 312 (2006) p.90.

[2] S. Kobayashi, Y. Tsukamoto, T. Takasugi, H. Chinen, T. Omori, K. Ishida, and S. Zaefferer, Intermetallics 17 (2009) p.1085.

[3] A. Suzuki, G. C. DeNolf, and T. M. Pollock, Scripta Mater. 56 (2007) p.385.

[4] A. Suzuki and T. M. Pollock, Acta Mater. 56 (2008) p.1288.

[5] K. Shinagawa, T. Omori, J. Sato, K. Oikawa, I. Ohnuma, R. Kainuma, and K. Ishida, Mater. Trans. 49 (2008) p.1474.

[6] K. Shinagawa, T. Omori, K. Oikawa, R. Kainuma, and K. Ishida, Scripta Mater. 61 (2009) p.612.

[7] M. Ooshima, K. Tanaka, N. L. Okamoto, K. Kishida, and H. Inui, J. Alloys Compd. 508 (2010) p.71.

[8] K. Tanaka, M. Ooshima, N. Tsuno, A. Sato, and H. Inui, Acta Mater. (to be submitted).

[9] K. Tanaka, T. Ohashi, K. Kishida, and H. Inui, Appl. Phys. Lett. 91 (2007) p.181907.

[10] Q. Yao, H. Xing, and J. Sun, Appl. Phys. Lett. 89 (2006) p.3.

[11] S. Miura, K. Ohkubo, and T. Mohri, Mater. Trans. 48 (2007) p.2403.

[12] P. Veyssière and D. G. Morris, Philos. Mag. A 67 (1993) p.491.

[13] D. J. Cockayne, I. L. F. Ray, and M. J. Whelan, Philos. Mag. 20 (1969) p.1265.

[14] J. Douin, http://pc-web.cemes.fr/Personnel/douin/Disdi-Page.html,

[15] B. Viguier, K. J. Hemker, and G. Vanderschaeve, Philos. Mag. A 69 (1994) p.19.

[16] P. Veyssière and J. Douin, *Dislocations*, in *Intermetallic Compounds Principles and Practice* Vol. 1, J. H. Westbrook and R. L. Fleischer, eds., John Wiley & Sons, Chichester, England, 1995, p. 519.

[17] Y. Q. Sun and P. M. Hazzledine, *Geometry of Dislocation Glide in $L1_2$ γ′-phase: TEM Observations*, in *Dislocations in Solids*, Vol. 10, F. R. N. Nabarro and M. S. Duesbery, eds., Elsevier, Amsterdam, 1996, p. 27.

[18] P. Veyssière and G. Saada, *Microscopy and plasticity of the $L1_2$ γ′ phase*, in *Dislocations in Solids*, Vol. 10, F. R. N. Nabarro and M. S. Duesbery, eds., Elsevier, Amsterdam, 1996, p. 253.

[19] Y. Liu, T. Takasugi, O. Izumi, and T. Takahashi, Philos. Mag. A 59 (1989) p.437.

[20] A. Couret, Y. Q. Sun, and P. B. Hirsch, Philos. Mag. A 67 (1993) p.29.

[21] M. Yamaguchi and Y. Umakoshi, Prog. Mater Sci. 34 (1990) p.1.

[22] C. T. Liu and D. P. Pope, *Ni_3Al and its Alloys*, in *Intermetallic Compounds Principles and Practice* Vol. 2, J. H. Westbrook and R. L. Fleischer, eds., John Wiley & Sons, Chichester, England, 1995, p. 17.
[23] T. Takasugi, S. Hirakawa, O. Izumi, S. Ono, and S. Watanabe, Acta Metall. 35 (1987) p.2015.
[24] Y. Oya-Seimiya, T. Shinoda, and T. Suzuki, Mater. Trans. JIM 37 (1996) p.1464.
[25] D. M. Wee, D. P. Pope, and V. Vitek, Acta Metall. 32 (1984) p.829.
[26] V. Vitek and V. Paidar, *Non-planar Dislocation Cores: A Ubiquitous Phenomenon Affecting Mechanical Properties of Crystalline Materials*, in *Dislocations in Solids*, Vol. 14, J. P. Hirth, eds., Elsevier, Amsterdam, 2008, p. 439.
[27] Z. L. Wu, D. P. Pope, and V. Vitek, Philos. Mag. A 70 (1994) p.159.
[28] U. F. Kocks, A. S. Argon, and M. F. Ashby, Prog. Mater Sci. 19 (1975) p.1.
[29] T. Wille and C. Schwink, Acta Metall. 34 (1986) p.1059.
[30] Y. Liu, T. Takasugi, O. Izumi, and T. Takahashi, Philos. Mag. A 59 (1989) p.423.
[31] D. G. Morris, R. Lerf, and M. Leboeuf, Acta Metall. Mater. 43 (1995) p.2825.
[32] V. Paidar, D. P. Pope, and M. Yamaguchi, Scripta Metall. 15 (1981) p.1029.
[33] P. Veyssière and G. Saada, *Microscopy and plasticity of the $L1_2$ γ' phase*, in *Dislocations in Solids*, Vol. 10, F. R. N. Nabarro and M. S. Duesbery, eds., Elsevier, Amsterdam, 1996, p. 253.
[34] M. H. Yoo, Scripta Metall. 20 (1986) p.915.
[35] K. J. Hemker and M. J. Mills, Philos. Mag. A 68 (1993) p.305.

Figure legend

Fig. 1. Typical SEM backscattered electron image of microstructure observed in an annealed ingot with a nominal composition of Co-12 at.%Al-11 at.%W.

Fig. 2. Selected stress-strain curves of $Co_3(Al,W)$ polycrystals obtained in compression at several different temperatures.

Fig. 3. Temperature dependence of yield stress of $Co_3(Al,W)$ polycrystals obtained in compression.

Fig. 4. Deformation markings observed on two orthogonal faces of two different grains (a), (b) A and (c),(d) B in a specimen deformed at 77 K to a plastic strain of about 2 %. The compression axis is in the vertical direction. Compression axis orientations for investigated grains are plotted in the stereographic projection (e).

Fig. 5. Deformation markings observed on two orthogonal faces of a grain in specimens deformed at (a,b) 873 K, (d,e) 1073 K, and (g,h) 1173 K, respectively. The compression axis is in the vertical direction. Compression axis orientations for investigated grains are plotted in the stereographic projections (c), (f) and (i), respectively.

Fig. 6. Typical dislocation structures observed in specimens deformed at (a) 77, (b) 159, (c) 300 and (d) 573 K, respectively. The thin foils were cut parallel to the (111) macroscopic slip plane.

Fig. 7. Weak-beam images of dislocations observed in a specimen deformed at 77 K. The reflection vectors used for imaging are indicated in each of the images.

Fig. 8. Corrected dissociation width between APB-coupled dislocations at 77 K plotted as a function of dislocation line direction with respect to the Burgers vector.

Fig. 9. Magnified weak-beam image of a faulted dipole indicated by a double arrow in fig. 6(b). The reflection vectors used for imaging are indicated in each of the images.

Fig. 10. Experimental bright- and dark-field images of a faulted dipole taken with $\boldsymbol{g} = \pm 1\bar{1}\,\bar{1}$ are shown in the first row. The corresponding images calculated with the assumption that the displacement vector ($\boldsymbol{R}_F$) is either +1/3[111] (intrinsic) or –1/3[111] (extrinsic) are shown in the second/third and fourth/fifth rows, respectively. The two partial dislocations bounding a stacking fault are assumed to have the same Burgers vector ($\boldsymbol{b}$ = 1/3[11$\bar{2}$] and 1/3[$\bar{1}\,\bar{1}$2] for the second/fourth and third/fifth rows, respectively) and opposite line vectors ($\boldsymbol{\xi}$ = [11$\bar{2}$] and [$\bar{1}\,\bar{1}$2] for the upper and lower partial dislocations, respectively).

Fig. 11. Typical dislocation structures observed in specimens deformed at (a) 973 and (b) 1073 K, respectively. The thin foils were cut parallel to the (111) macroscopic slip plane.

Fig. 12. (a)-(c) Weak-beam images of dislocations observed in a specimen deformed at 773 K. The reflection vectors used for imaging are indicated in each of the images. (d) Magnified image of a superkink connecting locked screw segments.

Fig. 13. Variation of the projected dissociation width for an APB-coupled dislocation observed in a specimen deformed at 773 K. The images were taken near (a) [010], (b) [121], (c) [111], and (d) [101] zone-axis orientations, respectively.

Fig. 14. (a) Typical dislocation structure observed in a specimen deformed at 1173 K. (b) Dark-field image taken with $\boldsymbol{g} = 001$, showing the existence of thermally formed APBs.

Fig. 15. Schematic illustration of the yield stress–temperature curve of $L1_2$ compounds.

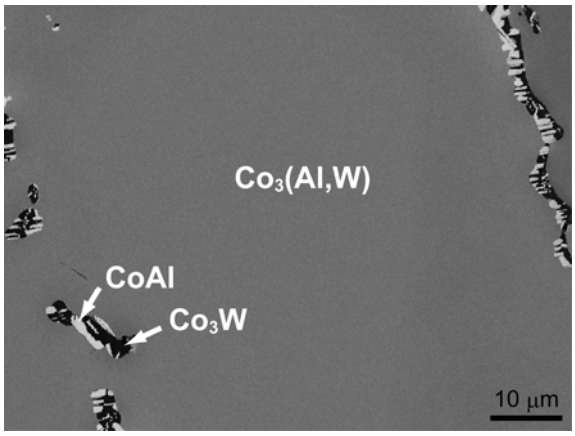

Figure 1.

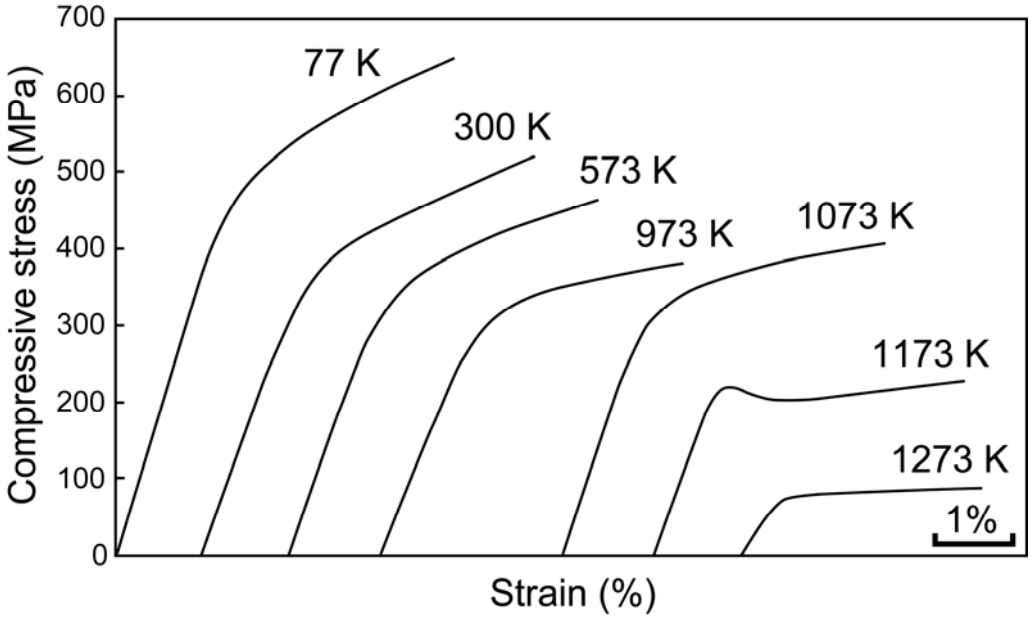

Figure 2.

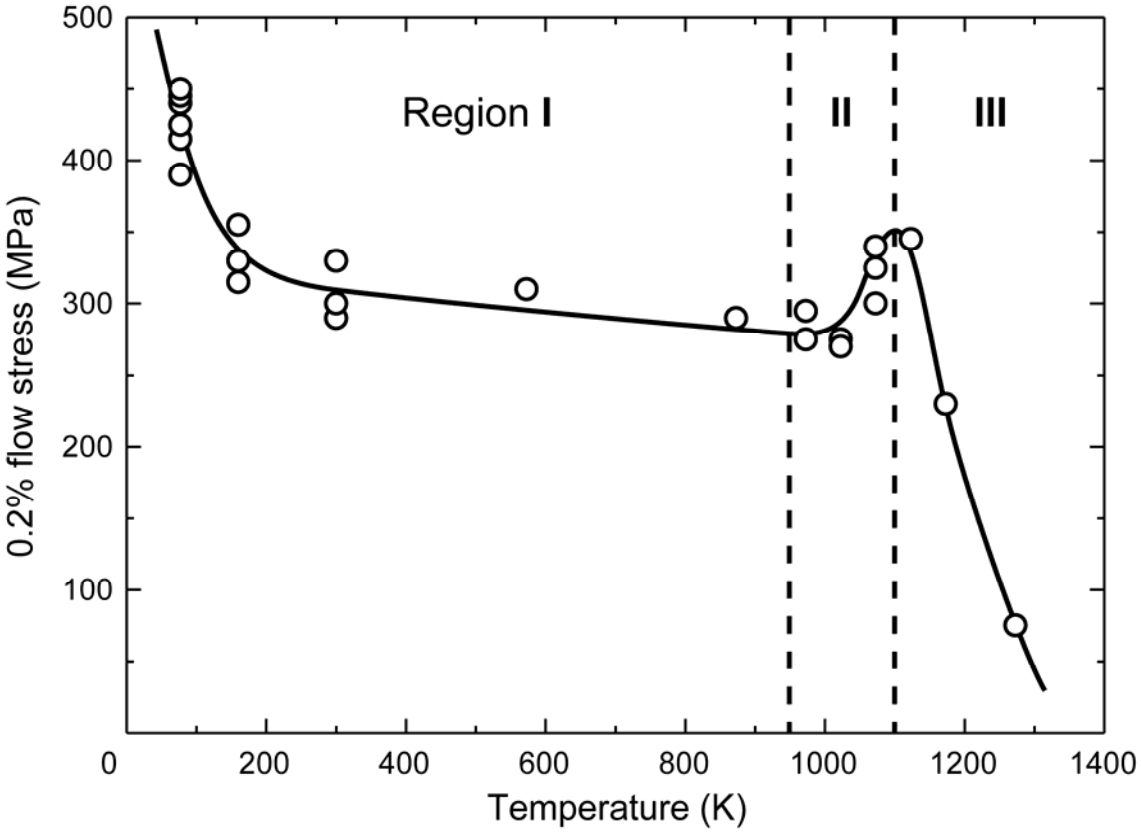

Figure 3.

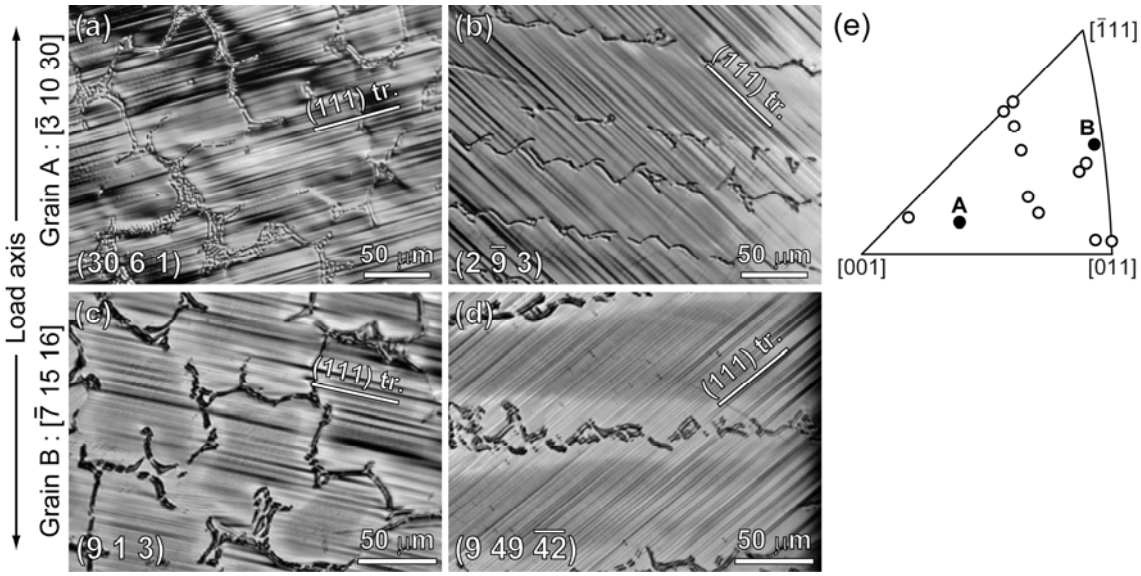

Figure 4.

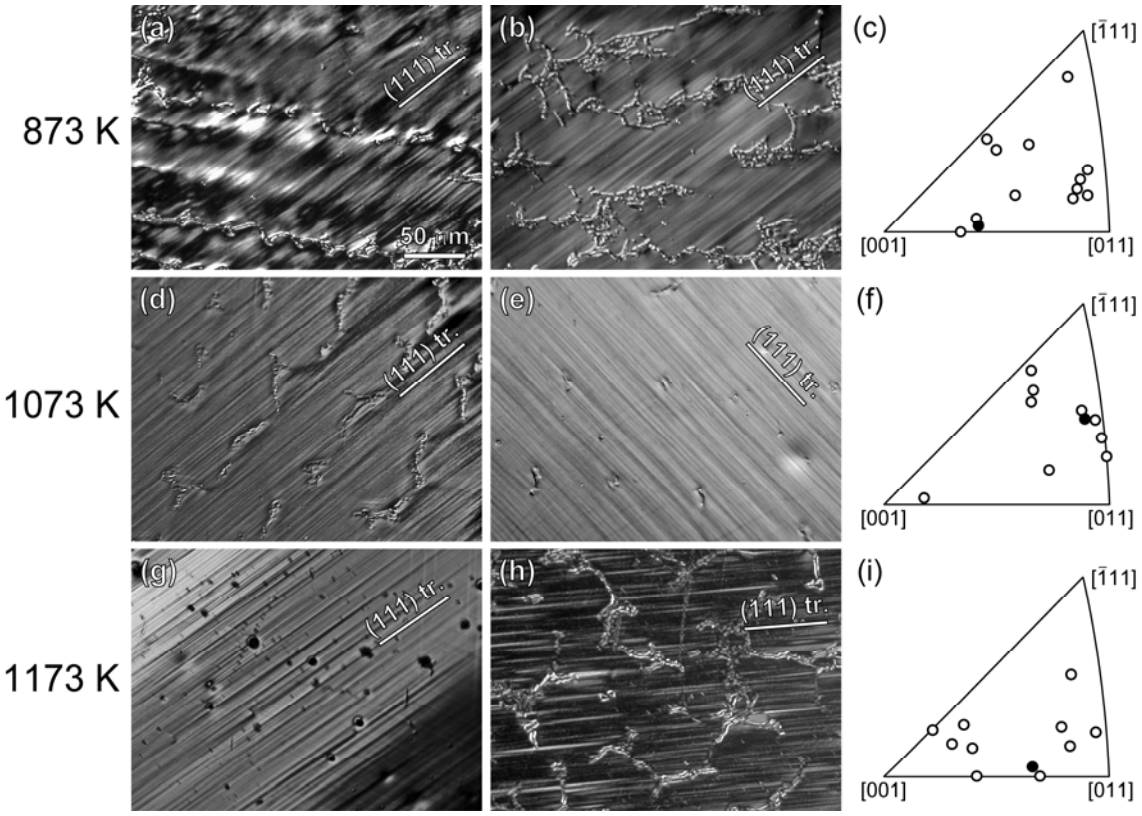

Figure 5.

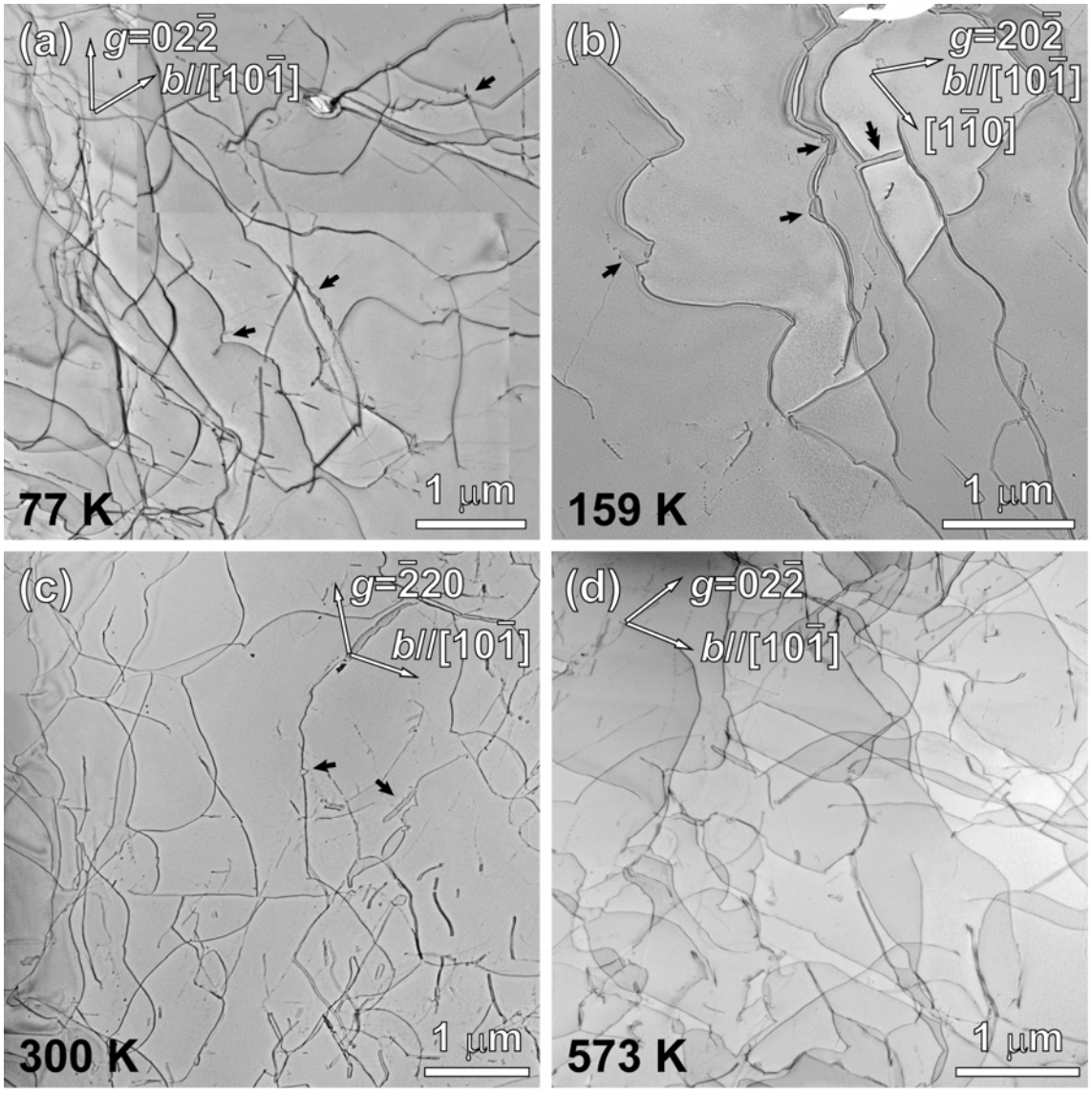
(a)
g=02$\bar{2}$
b//[10$\bar{1}$]
77 K
1 μm
(b)
g=20$\bar{2}$
b//[10$\bar{1}$]
[1$\bar{1}$0]
159 K
1 μm
(c)
g=$\bar{2}$20
b//[10$\bar{1}$]
300 K
1 μm
(d)
g=02$\bar{2}$
b//[10$\bar{1}$]
573 K
1 μm

Figure 6.

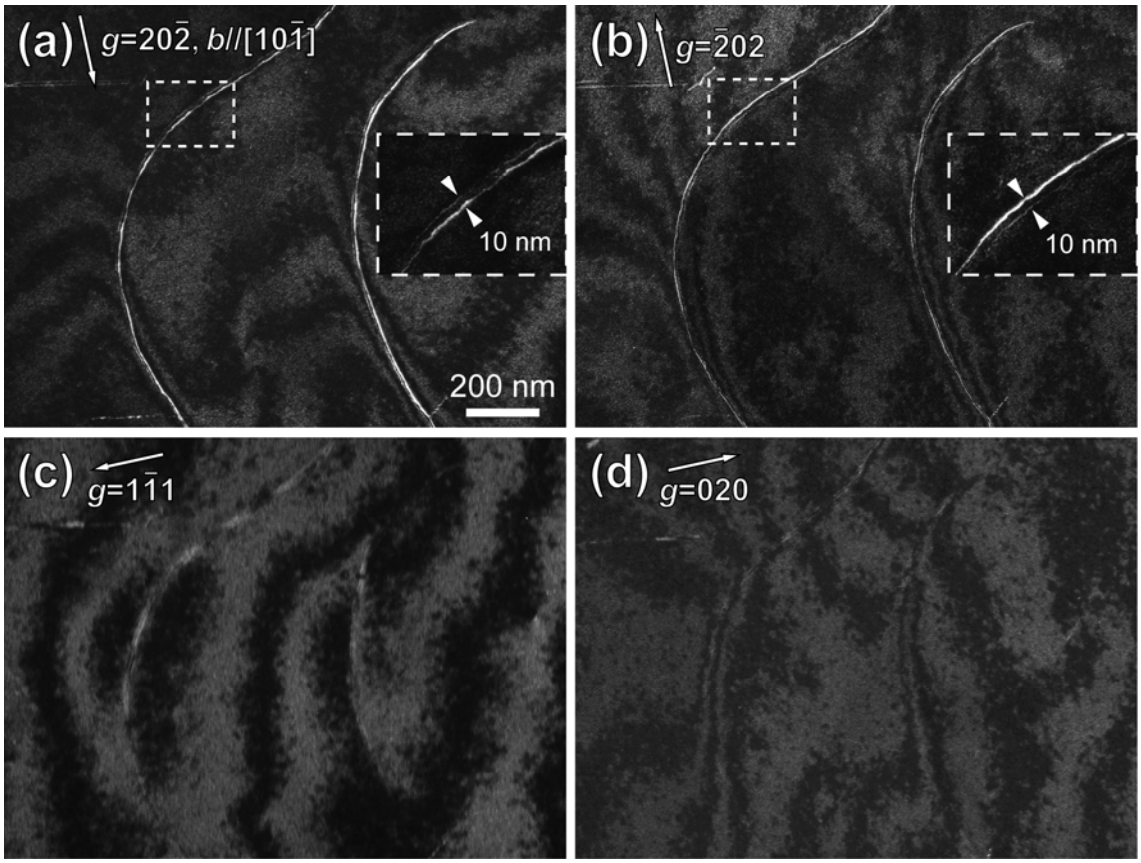

Figure 7.

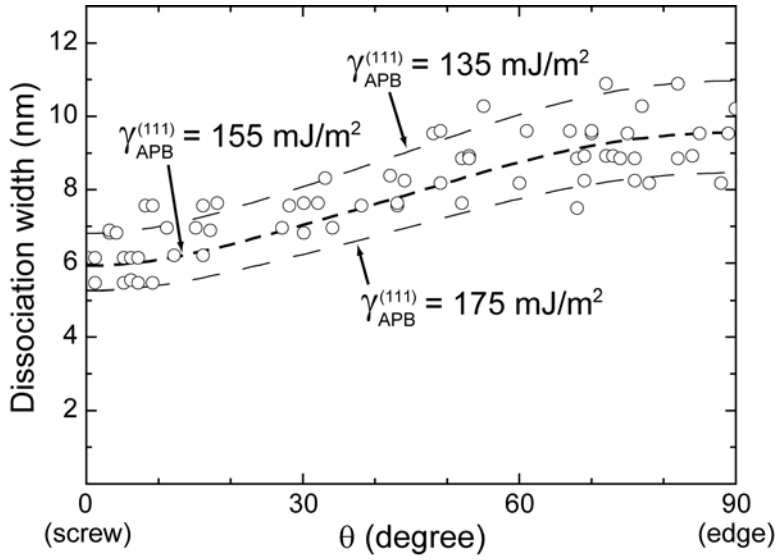

Figure 8.

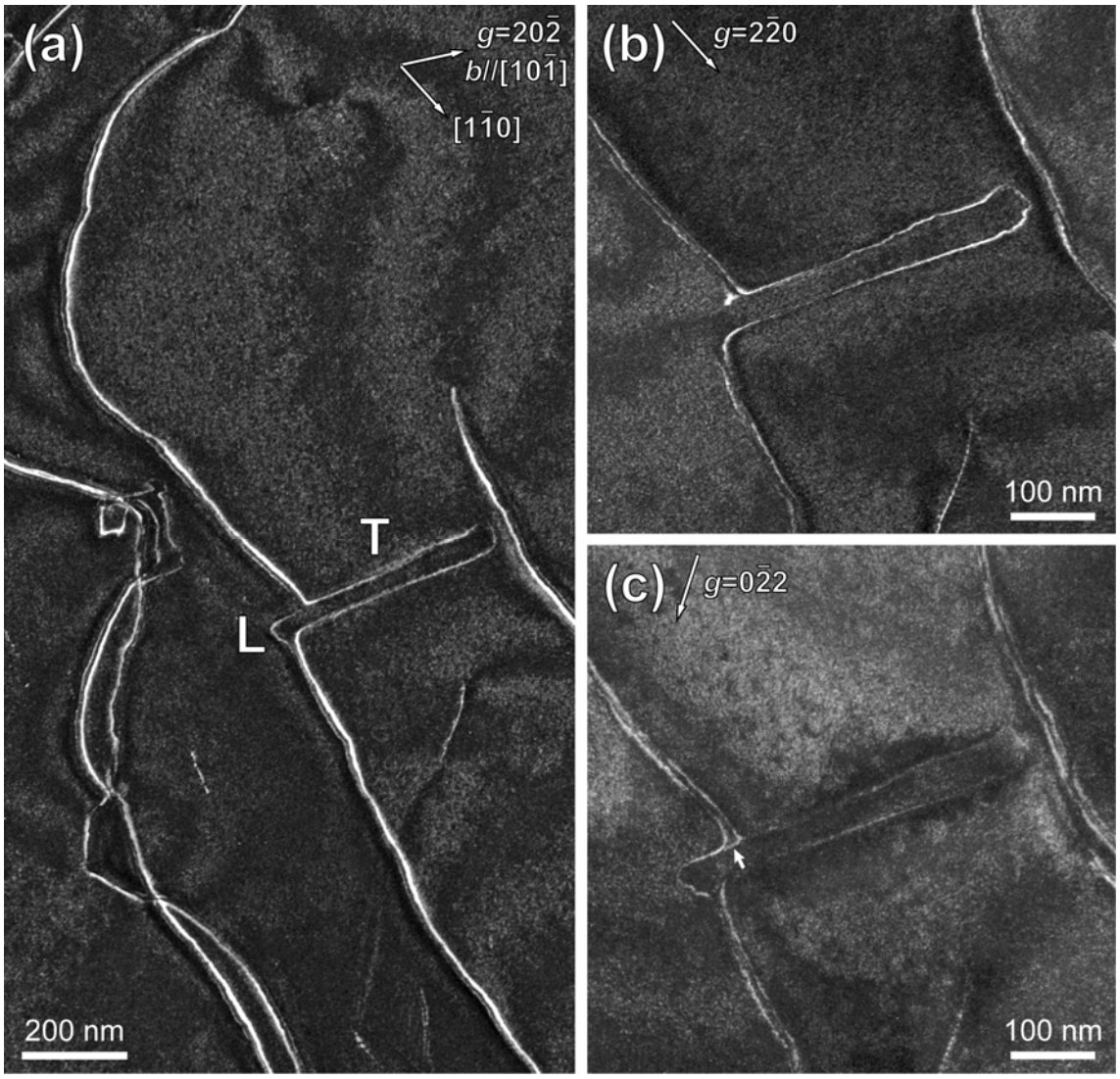
(a)
g=20$\bar{2}$
b//[10$\bar{1}$]
[1$\bar{1}$0]
T
L
200 nm
(b)
g=2$\bar{2}$0
100 nm
(c)
g=0$\bar{2}$2
100 nm

Figure 9.

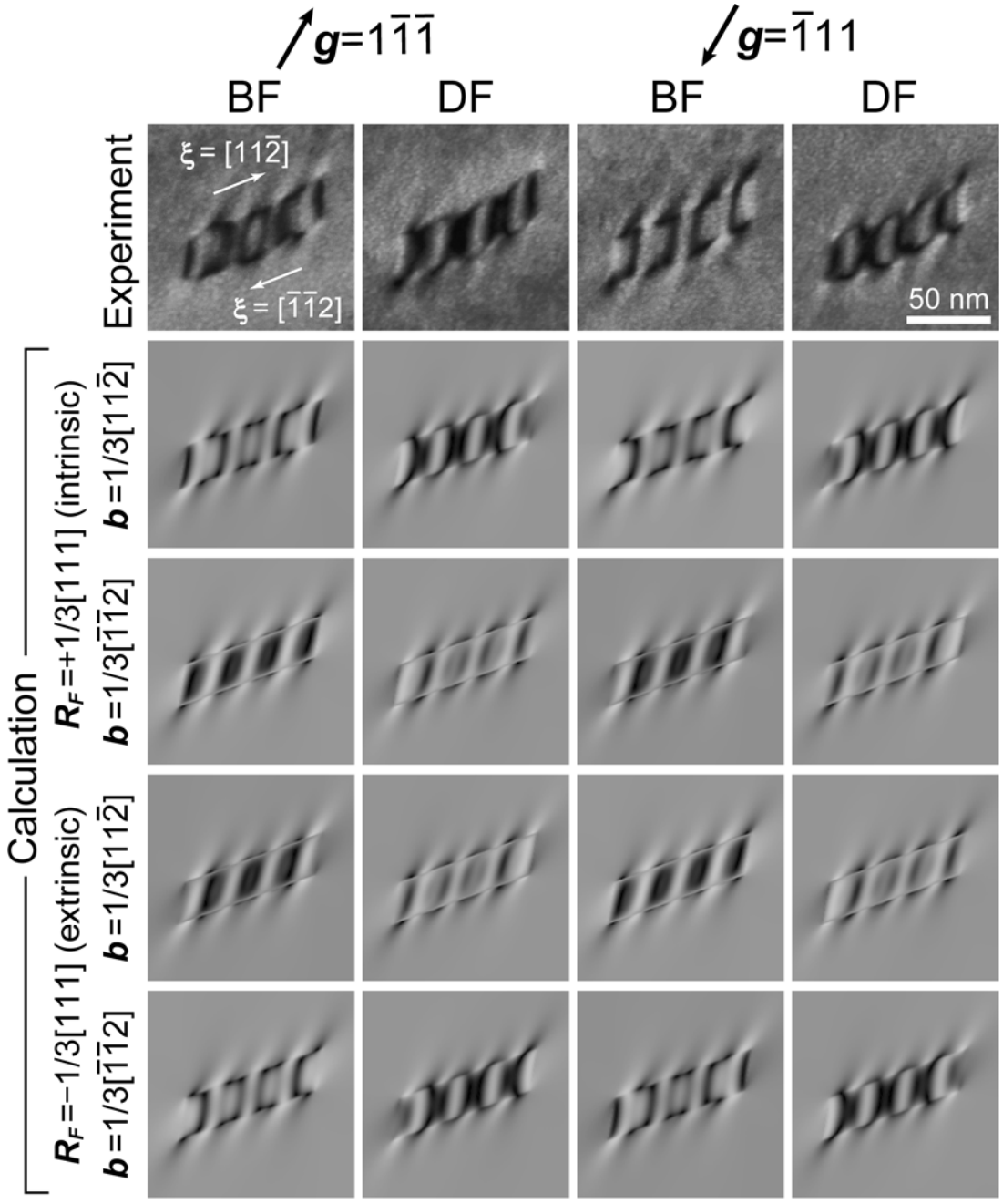
g=1$\bar{1}\bar{1}$
g=$\bar{1}$11
BF
DF
BF
DF
Experiment
ξ = [11$\bar{2}$]
ξ = [$\bar{1}\bar{1}$2]
50 nm
Calculation
R_F=+1/3[111] (intrinsic)
b=1/3[11$\bar{2}$]
b=1/3[$\bar{1}\bar{1}$2]
R_F=−1/3[111] (extrinsic)
b=1/3[11$\bar{2}$]
b=1/3[$\bar{1}\bar{1}$2]

Figure 10.

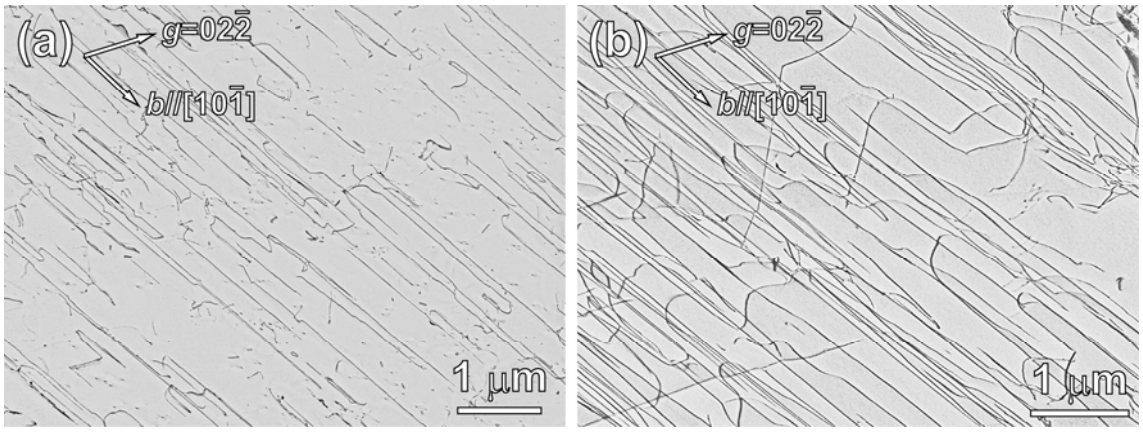

Figure 11.

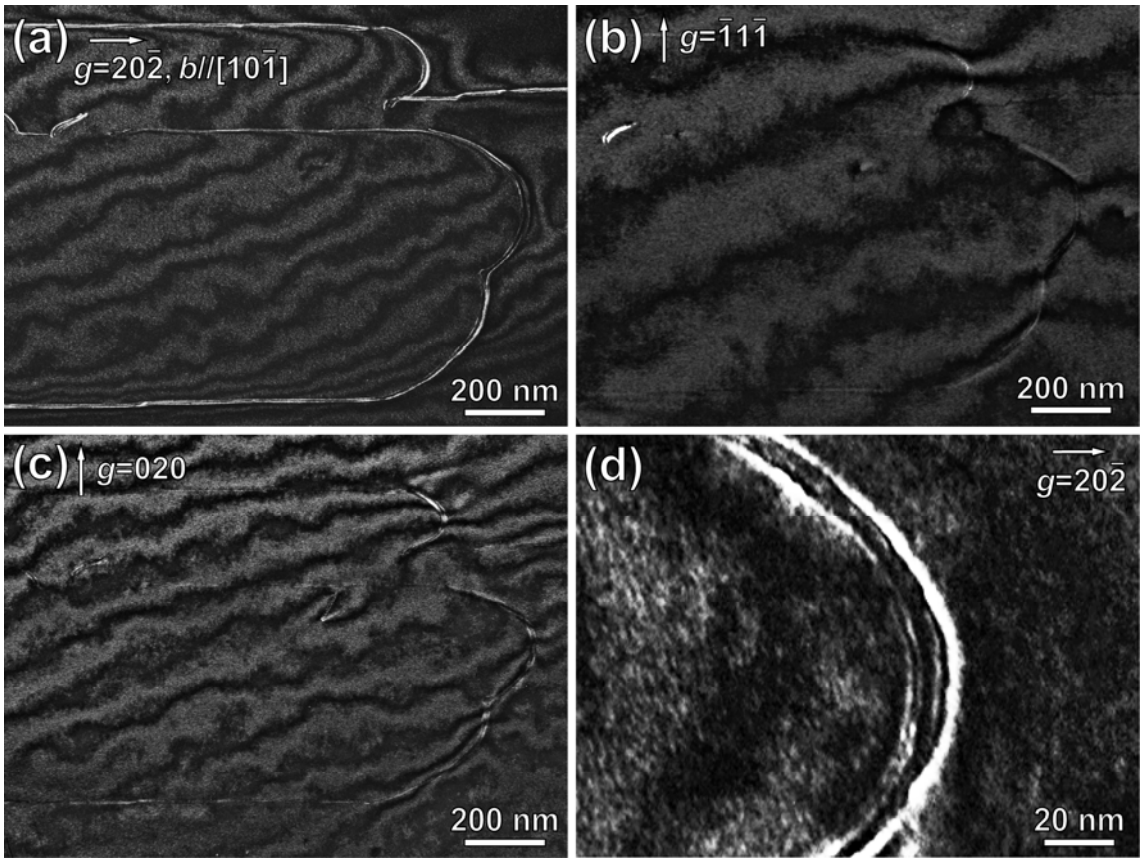

Figure 12.

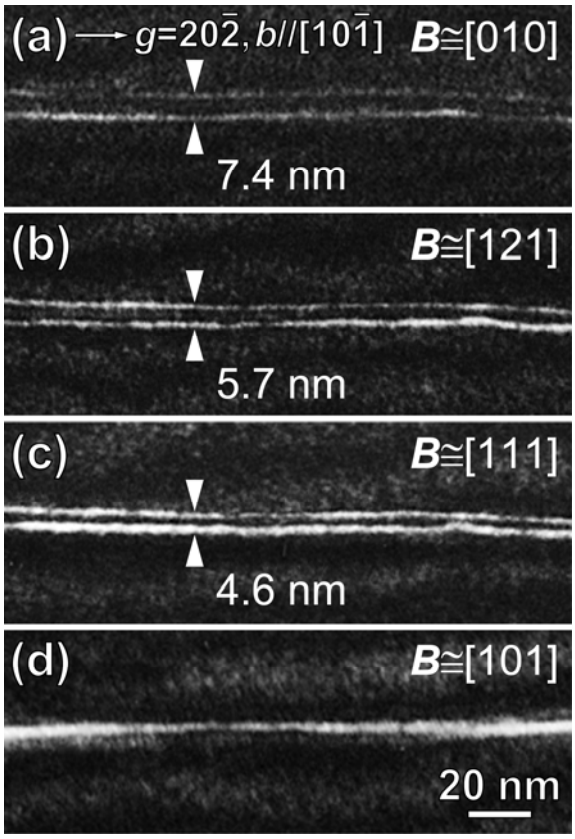

Figure 13.

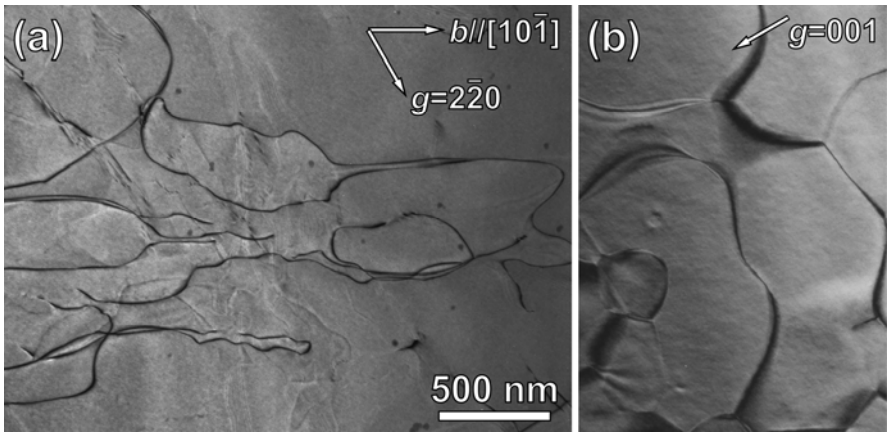

Figure 14.

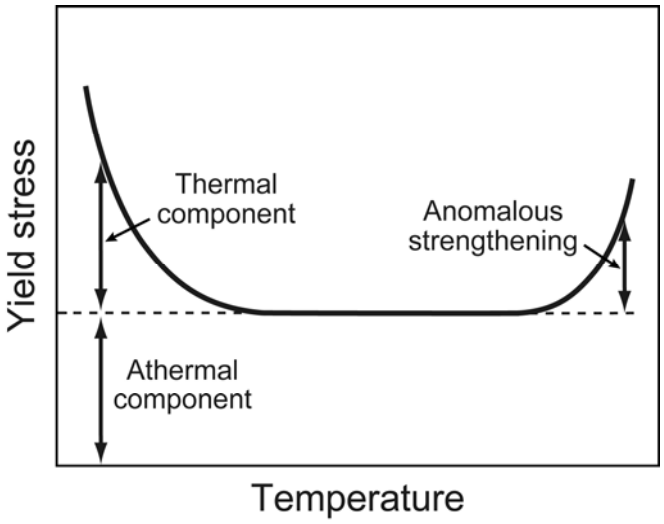
Yield stress
Thermal component
Anomalous strengthening
Athermal component
Temperature

Figure 15.